Structural Engineering and Mechanics, Vol. 40, No. 2 (2011) 167-190 167
DOI: http://dx.doi.org/10.12989/sem.2011.40.2.167

Characterization and shaking table tests of multiple trench friction pendulum system with numerous intermediate sliding plates

C.S. Tsai* and Yung-Chang Lin[a]

[1]*Department of Civil Engineering, Feng Chia University, Taichung, Taiwan*

(Received January 19, 2010, Revised March 23, 2011, Accepted August 17, 2011)

Abstract. In order to upgrade the seismic resistibility of structures and enhance the functionality of an isolator, a new base isolator called the multiple trench friction pendulum system (MTFPS) is proposed in this study. The proposed MTFPS isolator is composed of a trench concave surface and several intermediate sliding plates in two orthogonal directions. Mathematical formulations have been derived to examine the characteristics of the proposed MTFPS isolator possessing numerous intermediate sliding plates. By means of mathematical formulations which have been validated by experimental results of bidirectional ground shaking, it can be inferred that the natural period and damping effect of the MTFPS isolator with several intermediate sliding plates can be altered continually and controllably during earthquakes. Furthermore, results obtained from the component and shaking table tests demonstrate that the proposed isolator provides good protection to structures for prevention of damage from strong earthquakes.

Keywords: friction pendulum system; multiple friction pendulum system; base isolation; earthquake engineering; base isolator; trench friction pendulum system; sliding system

1. Introduction

The base isolation technology has been recognized as a promising technique for the prevention of existing and new structures from earthquake damage. Among the base isolators developed in the past, a friction pendulum system (FPS) isolation device with a concave sliding surface and an articulated slider was proposed by Zayas *et al.* (1987). Through extensive experimental and numerical studies, the FPS isolator has been proven to be an efficient device for reduction of the seismic responses of structures (Zayas *et al.* 1987, 1990, Al-Hussaini *et al.* 1994, Murnal and Sinha 2002, Mosqueda *et al.* 2004, Jangid 2005). In order to enhance the earthquake proof efficiency and reduce the size of the FPS isolator, a multiple friction pendulum system (MFPS) with double concave surfaces and an articulated slider located between the concave surfaces was proposed by Tsai *et al.* (2003) (Tsai *et al.* 2005, 2006). Seismic response characteristics of bridges using the multiple friction pendulum system with double concave surfaces have been reported by Kim and

*Corresponding author, Professor, E-mail: cstsai@fcu.edu.tw
[a]Ph.D. Candidate

Yun (2007). Furthermore, several other types of the MFPS isolator, which has numerous intermediate sliding plates and basically represent more than one pendulum system connected in series, were invented by Tsai (2002) (Tsai *et al.* 2008). Research conducted on the characteristics of the MFPS isolator with four sliding surfaces (two intermediate sliding plates) has been published by Fenz and Constantinou (2008). The efficiency of the MFPS isolator with four concave surfaces on seismic mitigation of buildings has been investigated by Morgan and Mahin (2008). A direction-optimized friction pendulum system (DO-FPS) consisting of a spherical concave surface, a trench concave surface, and an articulated slider has been developed by Tsai *et al.* (2008). The DO-FPS isolator possesses important characteristics such as the natural period and damping effect, which are functions of the directional angle of the sliding motion of the articulated slider during earthquakes. An isolation system, called the *X-Y* isolator, consisting of two orthogonal concave beams interconnected through a sliding mechanism has been published by Roussis and Constantinou (2006). Furthermore, a trench friction pendulum system (TFPS) that consists of one trench concave surface in the x and y directions and an articulated slider situated between the trench concave surfaces has been proposed by Tsai *et al.* (2010a). The TFPS possesses independent characteristics such as the natural period and damping effect in two orthogonal directions, which can be applied to a bridge or a structure with considerably different natural periods in two orthogonal directions.

In order to further enhance the functionality of the TFPS isolator (Tsai *et al.* 2010a), a new base isolation system called the multiple trench friction pendulum system (MTFPS) with numerous intermediate sliding plates is proposed in this study. As shown in Figs. 1-3, the MTFPS isolator has

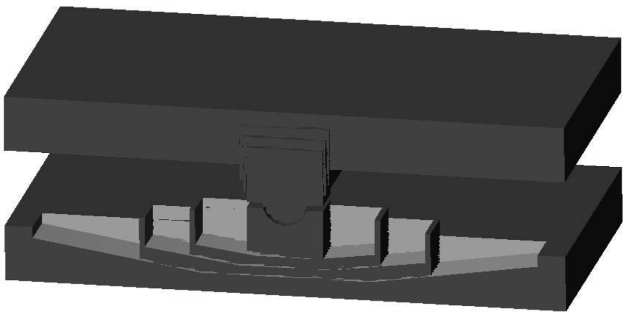

Fig. 1 Cross sectional view of multiple trench friction pendulum system

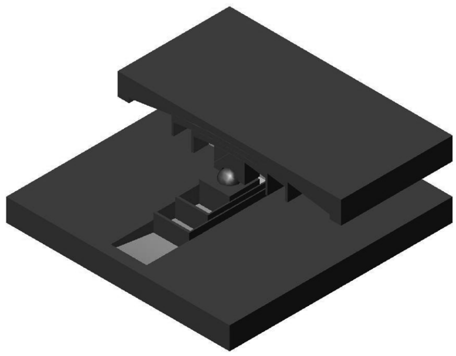

Fig. 2 Exploded view of MTFPS Isolator

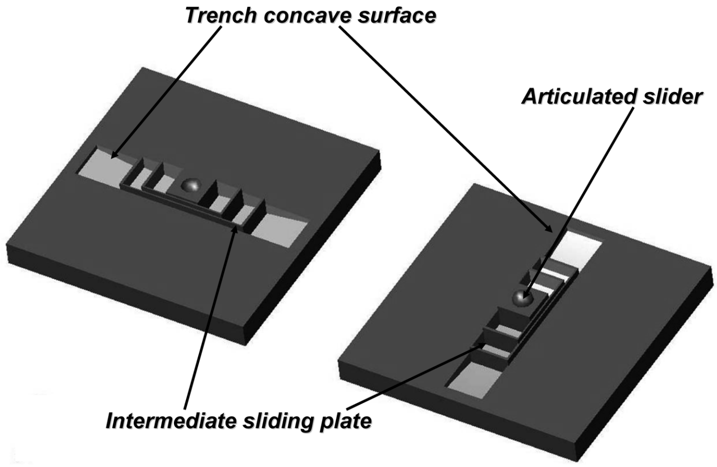

Fig. 3 Open-up view of MTFPS Isolator

multiple concave sliding interfaces that are composed of a trench concave surface, several intermediate sliding plates in each orthogonal direction, and an articulated slider located among the trench concave surfaces and intermediate sliding plates. The MTFPS represents more than one trench friction pendulum system connected in series in each orthogonal direction. The friction coefficient, displacement capacity, and radius of curvature of each trench concave surface or intermediate sliding plate in each direction can be different. The natural period and damping effect for a MTFPS isolator with several intermediate sliding plates change continually during earthquakes. Therefore, a large number of possibilities of combinations are available for engineering designs. Such options are dependent on the engineering requirements. In order to examine the features of the new device, mathematical formulations, which have been verified by experimental results of bidirectional ground shaking, have been derived in this study; to investigate the efficiency of the proposed MTFPS isolator in seismic mitigation for structures, a series of shaking table tests for a scaled steel structure equipped with the MTFPS isolators were carried out in the Department of Civil Engineering, Feng Chia University, Taichung, Taiwan. The results obtained from the experimental tests demonstrate that the MTFPS isolator with numerous intermediate sliding plates provides good protection for structures from earthquake damage. Furthermore, a comparison of mechanical features between the MTFPS isolator and the MFPS isolator with several sliding interfaces (Tsai *et al.* 2010b) has been made while the systems are subjected to bidirectional ground accelerations.

2. Mathematical formulations for MTFPS isolator with numerous intermediate sliding plates

In order to study the characteristic of the MTFPS isolator with numerous intermediate sliding plates, mathematical formulations have been derived as follows. Fig. 4 shows a MTFPS isolator having one trench concave surface and two intermediate sliding plates to form three sliding interfaces in the X direction. The effective radii of curvature of the first, second, and third sliding interfaces are R_{x1}, R_{x2}, and R_{x3}, respectively (Fenz and Constantinou 2008). The friction coefficients

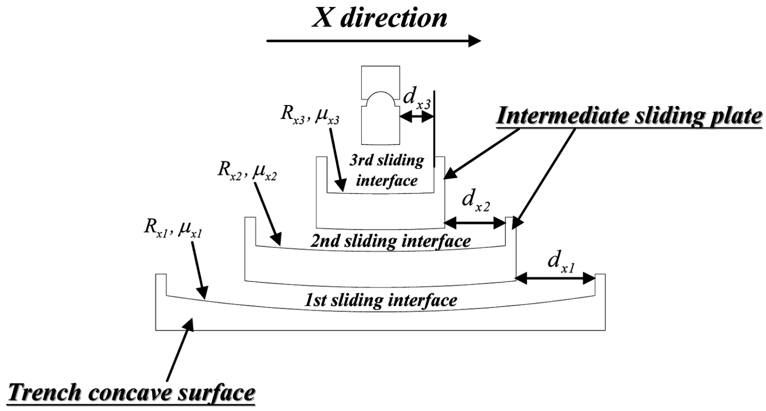

Fig. 4 Properties of sliding interfaces in MTFPS isolator

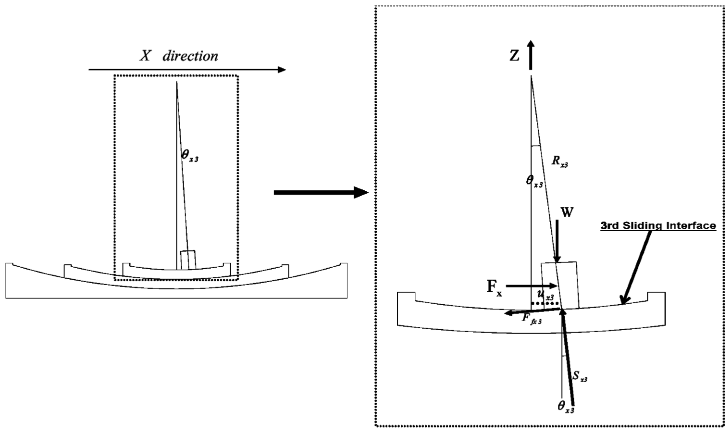

Fig. 5 Displaced positions (a) free body diagram of MTFPS during sliding Stage I in X-direction, and (b) sliding occurrence on third sliding interface

of the first, second, and third sliding interfaces are μ_{x1}, μ_{x2}, and μ_{x3}, respectively. The displacement capacities on the first, second, and third sliding interfaces are d_{x1}, d_{x2}, and d_{x3}, respectively. In the following derivations, we assume the following conditions: (a) $R_{x1} > R_{x2} > R_{x3}$; (b) $\mu_{x1} > \mu_{x2} > \mu_{x3}$; and (c) $d_{xi} > (\mu_{x(i-1)} - \mu_{xi})R_{xi}$. Figs. 5(a) and (b) show the forces acting on the third sliding interface in the X direction when the sliding motion is initiated on the third sliding interface with the least friction coefficient. F_x denotes the mobilized force in the X direction; u_x, the total displacement of the articulated slider in the X direction; u_{xi}, the displacement on the i-th sliding interface in the X-direction; S_{xi}, the force normal to the i-th sliding interface in the X-direction; F_{fxi}, the frictional force in the direction tangential to the i-th sliding interface; W, the vertical force resulting from the superstructure including the static and dynamic loadings; and θ_{xi}, the rotation angle in the X-direction on the i-th sliding interface relative to the vertical direction. The sliding sequence of the components of the MTFPS isolator is determined by the friction coefficients and the radii of the sliding interfaces. The sliding motion is initiated on the i-th sliding interface when the horizontally mobilized force, F_x, exceeds the frictional force on the i-th sliding interface, F_{fxi}.

In stage I, when $F_{fx3} \leqq F_x < F_{fx2}$, the articulated slider starts sliding on the third sliding interface. As shown in Figs. 5(a) and (b), from the equilibrium equation in the *X*-direction and by neglecting the frictional forces from the walls of intermediate plates, the governing equation in the horizontal direction is expressed as

$$F_x - S_{x3}\sin\theta_{x3} - F_{fx3}\cos\theta_{x3} = 0 \tag{1}$$

The governing equation in the vertical direction is obtained as

$$W - S_{x3}\cos\theta_{x3} + F_{fx3}\sin\theta_{x3} = 0 \tag{2}$$

Rearrangement of Eq. (2) results in the following expression

$$S_{x3} = \frac{W + F_{fx3}\sin\theta_{x3}}{\cos\theta_{x3}} \tag{3}$$

Back-substitution of Eq. (3) into Eq. (1) leads to

$$F_x = W\tan\theta_{x3} + \frac{F_{fx3}}{\cos\theta_{x3}} = W\frac{\sin\theta_{x3}}{\cos\theta_{x3}} + \frac{F_{fx3}}{\cos\theta_{x3}} \tag{4}$$

If the displacement is small, i.e., if $\theta_{x3} \approx 0$ and $\cos\theta_{x3} \approx 1$, Eq. (4) can be rewritten as follows

$$F_x = W\sin\theta_3 + F_{fx3} = \frac{W}{R_{x3}}u_{x3} + F_{fx3} \tag{5}$$

where

$$\sin\theta_{x3} = \frac{u_{x3}}{R_{x3}} \tag{6}$$

The total displacement in the X direction is obtained as $u_x = u_{x1} + u_{x2} + u_{x3} = 0 + 0 + u_{x3}$.
Eq. (5) can be rewritten as

$$F_x = \frac{W}{R_{x3}}u_x + F_{fx3} \tag{7}$$

and the hysteretic behavior of the MTFPS isolator is illustrated in Fig. 6.

In stage II, as shown in Fig. 7, when $F_x = F_{fx2}$, the sliding motion on the third sliding interface will stop, and the second sliding interface will start sliding.

The mobilized force under such conditions is expressed as follows

$$F_x = \frac{W}{R_{x3}}u_x + F_{fx3} = F_{fx2} \tag{8}$$

and the transition action occurs at displacement u_x^*, expressed by

$$u_x^* = (F_{fx2} - F_{fx3})\frac{R_{x3}}{W} = (\mu_{x2} - \mu_{x3})R_{x3} \tag{9}$$

When $F_{fx2} \leqq F_x < F_{fx1}$ the mobilized force on the second sliding interface is given by

$$F_x = \frac{W}{R_{x2}}u_{x2} + F_{fx2} \tag{10}$$

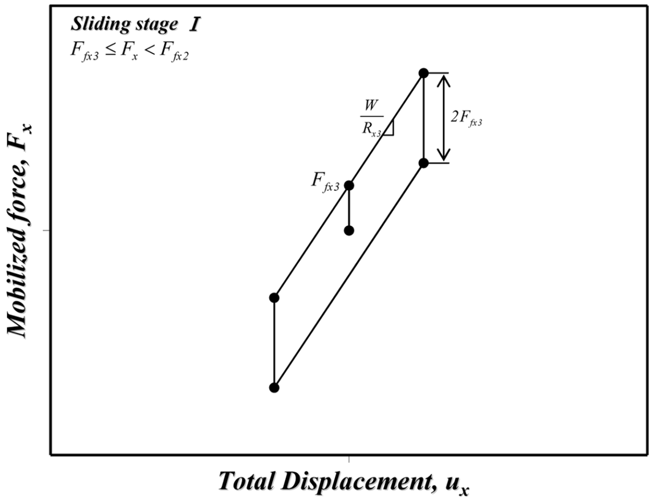

Fig. 6 Force-displacement relationship of the MTFPS isolator during Stage I

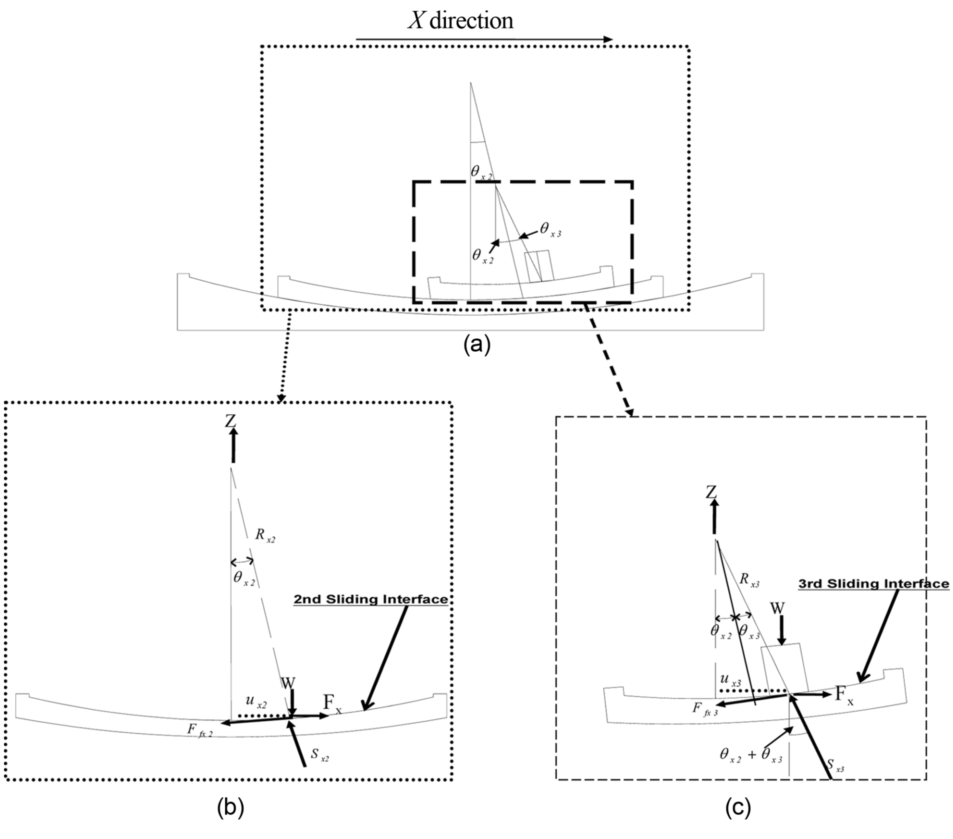

Fig. 7 Displaced positions (a) free body diagram of the MTFPS during sliding Stage II in X-direction, (b) sliding occurrence on second sliding interface, and (c) a constant displacement on third sliding interface

On the third sliding interface, the governing equation in the horizontal direction is expressed as

$$F_x - S_{x3}\sin(\theta_{x2} + \theta_{x3}) - F_{fx3}\cos(\theta_{x2} + \theta_{x3}) = 0 \tag{11}$$

and the governing equation in the vertical direction is obtained as

$$W - S_{x3}\cos(\theta_{x2} + \theta_{x3}) + F_{fx3}\sin(\theta_{x2} + \theta_{x3}) = 0 \tag{12}$$

The solution to Eqs. (12) and (13) is given by

$$\begin{aligned} F_x &= W\tan(\theta_{x2} + \theta_{x3}) + \frac{F_{fx3}}{\cos(\theta_{x2} + \theta_{x3})} \\ &= W\frac{\sin(\theta_{x2} + \theta_{x3})}{\cos(\theta_{x2} + \theta_{x3})} + \frac{F_{fx3}}{\cos(\theta_{x2} + \theta_{x3})} \end{aligned} \tag{13}$$

If the displacement is small, i.e., if $\theta_{x2} \approx \theta_{x3} \approx 0$, then, $\cos\theta_{x2} \approx \cos\theta_{x3} \approx 1$ and $\sin\theta_{x2}\sin\theta_{x3} \approx 0$. Eq. (13) can be rewritten as

$$F_x = W(\sin\theta_{x2} + \sin\theta_{x3}) + F_{fx3} = W\left(\frac{u_{x2}}{R_{x2}} + \frac{u_{x3}}{R_{x3}}\right) + F_{fx3} \tag{14}$$

Substitution of Eq. (10) into Eq. (14) yields

$$u_{x3} = (F_{fx2} - F_{fx3})\frac{R_{x3}}{W} = (\mu_{x2} - \mu_{x3})R_{x3} \tag{15}$$

= constant if the effect of velocity dependence on the friction coefficient is neglected.

The result in Eq. (15) implies that the displacement on the third sliding interface is constant and that the sliding motion on the third sliding interface stops in this stage.

Substitution of Eq. (15) into Eq. (14) yields

$$u_{x2} = (F_x - \mu_{x2}W)\frac{R_{x2}}{W} = (F_x - F_{fx2})\frac{R_{x2}}{W} \tag{16}$$

The total displacement is obtained as $u_x = u_{x1} + u_{x2} + u_{x3} = 0 + u_{x2} + u_{x3}$ in the X direction, and rearrangement of Eqs. (15) and (16) yields

$$\begin{aligned} F_x &= \frac{W}{R_{x2}}[u_x - u_{x1} - u_{x3}] + F_{fx2} \\ &= \frac{W}{R_{x2}}[u_x - (\mu_{x2} - \mu_{x3})R_{x3}] + F_{fx2} \\ &= \frac{W}{R_{x2}}u_x + \left[\frac{F_{fx2}(R_{x2} - R_{x3}) + F_{fx3}R_{x3}}{R_{x2}}\right] \end{aligned} \tag{17}$$

The hysteretic behavior of the MTFPS isolator in this stage is demonstrated in Fig. 8.

In stage III, as shown in Fig. 9, when $F_x = F_{fx1}$, the sliding motion on the second sliding interface stops and the first sliding interface starts sliding.

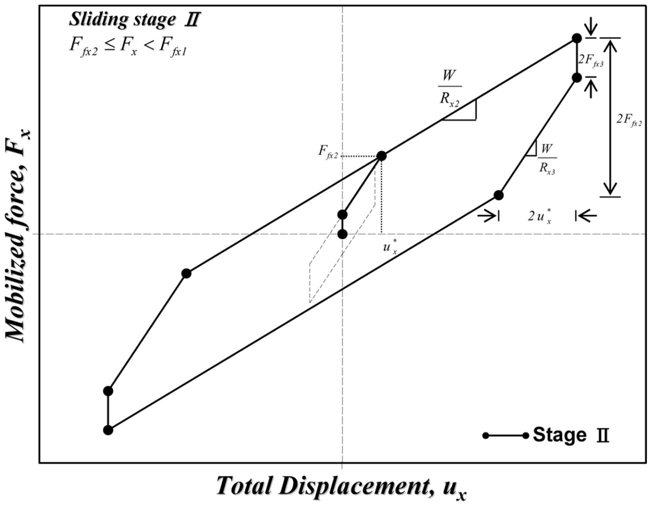

Fig. 8 Force-displacement relationship of the MTFPS isolator during Stage II

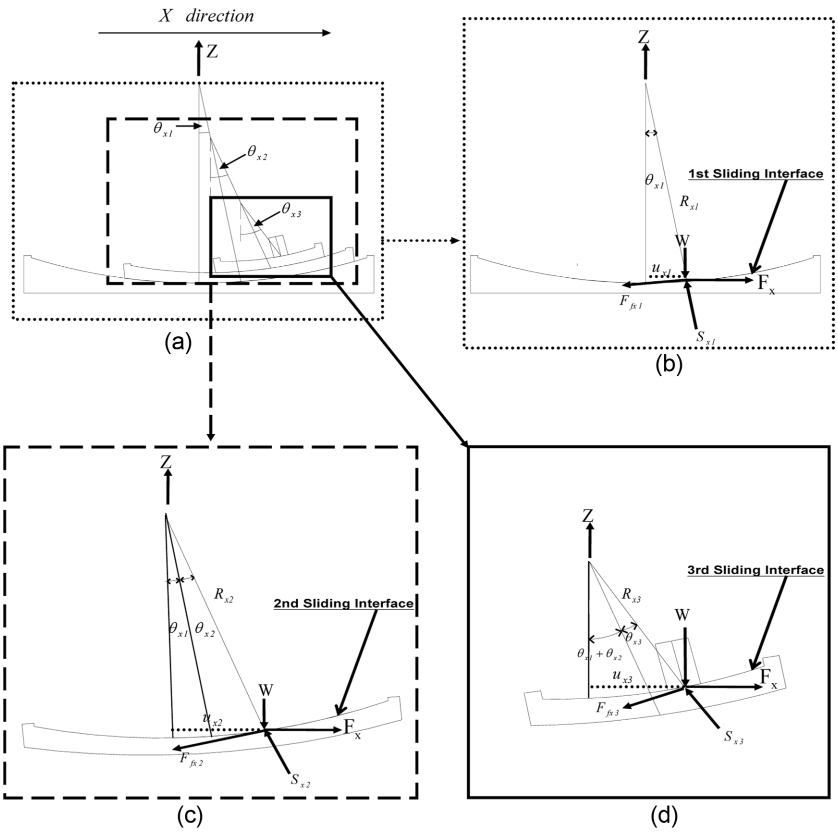

Fig. 9 Displaced positions (a) free body diagram of the MTFPS during sliding Stage III in *X*-direction (b) sliding occurrence on first sliding interface, (c) a constant displacement on second sliding interface, and (d) a constant displacement on third sliding interface

By using Eq. (17), the mobilized force under the abovementioned conditions is obtained as

$$F_{fx1} = \frac{W}{R_{x2}}u_x + \frac{F_{fx2}(R_{x2} - R_{x3}) + F_{fx3}R_{x3}}{R_{x2}} \tag{18}$$

and this transition action occurs at displacement u_x^{**}, expressed as

$$\begin{aligned} u_x^{**} &= \left[F_{fx1} - \frac{F_{fx2}(R_{x2} - R_{x3}) + F_{fx3}R_{x3}}{R_{x2}}\right]\frac{R_{x2}}{W} \\ &= (\mu_{x1} - \mu_{x2})R_{x2} + (\mu_{x2} - \mu_{x3})R_{x3} \end{aligned} \tag{19}$$

When $F_{fx1} \leqq F_x$ the mobilized force on the first interface is obtained as

$$F_x = \frac{W}{R_{x1}}u_{x1} + F_{fx1} \tag{20}$$

As shown in Fig. 9(c), on the second sliding interface, the governing equation in the horizontal direction is expressed as follows

$$F_x - S_{x2}\sin(\theta_{x1} + \theta_{x2}) - F_{fx2}\cos(\theta_{x1} + \theta_{x2}) = 0 \tag{21}$$

and the governing equation in the vertical direction is obtained as

$$W - S_{x2}\cos(\theta_{x1} + \theta_{x2}) + F_{fx2}\sin(\theta_{x1} + \theta_{x2}) = 0 \tag{22}$$

The solution to Eqs. (21) and (22) is expressed as

$$F_x = W\sin(\theta_{x1} + \theta_{x2}) + F_{fx2} = W\left(\frac{u_{x1}}{R_{x1}} + \frac{u_{x2}}{R_{x2}}\right) + F_{fx2} \tag{23}$$

As shown in Fig. 9(d), on the third sliding interface, the governing equation in the horizontal direction is given by

$$F_x - S_{x3}\sin(\theta_{x1} + \theta_{x2} + \theta_{x3}) - F_{fx3}\cos(\theta_{x1} + \theta_{x2} + \theta_{x3}) = 0 \tag{24}$$

and the governing equation in the vertical direction is obtained as

$$W - S_{x3}\cos(\theta_{x1} + \theta_{x2} + \theta_{x3}) + F_{fx3}\sin(\theta_{x1} + \theta_{x2} + \theta_{x3}) = 0 \tag{25}$$

Combining Eqs. (25) and (26) yields

$$\begin{aligned} F_x &= W\tan(\theta_{x1} + \theta_{x2} + \theta_{x3}) + \frac{F_{fx3}}{\cos(\theta_{x1} + \theta_{x2} + \theta_{x3})} \\ &= W\frac{\sin(\theta_{x1} + \theta_{x2} + \theta_{x3})}{\cos(\theta_{x1} + \theta_{x2} + \theta_{x3})} + \frac{F_{fx3}}{\cos(\theta_{x1} + \theta_{x2} + \theta_{x3})} \end{aligned} \tag{26}$$

For small displacements, Eq. (26) can be rewritten as

$$\begin{aligned} F_x &= W(\sin\theta_{x1} + \sin\theta_{x2} + \sin\theta_{x3}) + F_{fx3} \\ &= W\left(\frac{u_{x1}}{R_{x1}} + \frac{u_{x2}}{R_{x2}} + \frac{u_{x3}}{R_{x3}}\right) + F_{fx3} \end{aligned} \tag{27}$$

Substitution of Eq. (23) into Eq. (27) yields

$$u_{x3} = (F_{fx2} - F_{fx3})\frac{R_{x3}}{W} = (\mu_{x2} - \mu_{x3})R_{x3} \tag{28}$$

Substitution of Eq. (20) into Eq. (23) leads to

$$u_{x2} = (F_{fx1} - F_{fx2})\frac{R_{x2}}{W} = (\mu_{x1} - \mu_{x2})R_{x2} \tag{29}$$

The total displacement in the X direction is obtained as $u_x = u_{x1} + u_{x2} + u_{x3}$
Combination of Eqs. (20), (28), and (29) results in

$$F_x = \frac{W}{R_{x1}}[u_x - u_{x2} - u_{x3}] + F_{fx1}$$

$$= \frac{W}{R_{x1}}u_x + \frac{F_{fx1}(R_{x1} - R_{x2}) + F_{fx2}(R_{x2} - R_{x3}) + F_{fx3}R_{x3}}{R_{x1}} \tag{30}$$

The hysteretic behavior of the MTFPS isolator in this stage is shown in Fig. 10.

In stage IV, when contact is made with the displacement restrainer on the first sliding interface, the sliding motion on the first sliding interface stops and the sliding of the second sliding interface is restarted. The displacement on the first sliding interface, u_{x1}, is equal to d_{x1} and the mobilized force, F_{xdr1}, under such conditions is given by

$$F_{xdr1} = \frac{W}{R_{x1}}d_{x1} + F_{fx1} \tag{31}$$

This transition action occurs at the total displacement, u_{xdr1}, expressed as

$$u_{xdr1} = d_{x1} + u_{x2} + u_{x3}$$

$$= d_{x1} + (\mu_{x1} - \mu_{x2})R_{x2} + (\mu_{x2} - \mu_{x3})R_{x3} \tag{32}$$

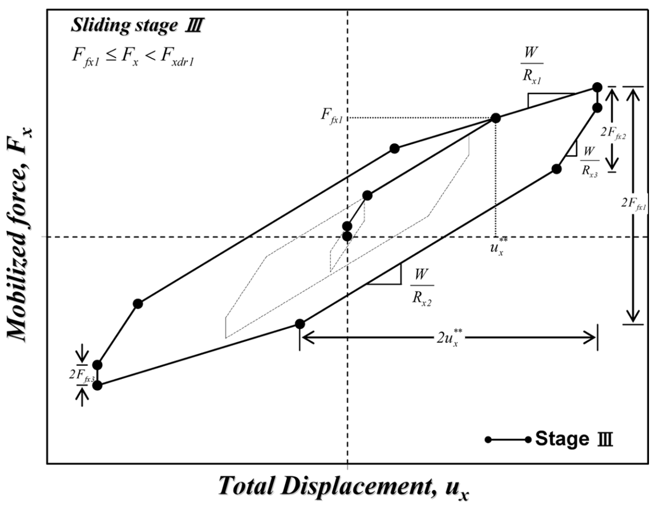

Fig. 10 Force-displacement relationship of the MTFPS isolator during Stage III

After the contact, the mobilized force on the second sliding interface is obtained as

$$F_x = W\left(\frac{d_{x1}}{R_{x1}} + \frac{u_{x2}}{R_{x2}}\right) + F_{fx2} \tag{33}$$

The mobilized force on the third sliding interface is given by

$$F_x = W\left(\frac{d_{x1}}{R_{x1}} + \frac{u_{x2}}{R_{x2}} + \frac{u_{x3}}{R_{x3}}\right) + F_{f3} \tag{34}$$

Back-substitution of Eq. (34) into Eq. (33) leads to

$$u_{x3} = \frac{R_{x3}}{W}(F_{fx2} - F_{fx3}) = (\mu_{x2} - \mu_{x3})R_{x3} \tag{35}$$

Note that the displacement on the third sliding interface given by Eq. (35) is a constant value in this stage, the third sliding interface remains motionless, and sliding motion occurs on the second sliding interface.

The total displacement $u_x = u_{x1} + u_{x2} + u_{x3}$; therefore, $u_{x2} = u_x - d_{x1} - u_{x3}$, and back-substitution of Eq. (35) into Eq. (33) leads to

$$\begin{aligned} F_x &= \frac{W}{R_{x2}}[u_x - u_{x1} - u_{x3}] + W\frac{d_{x1}}{R_{x1}} + F_{fx2} \\ &= \frac{W}{R_{x2}}[u_x - d_{x1} - (\mu_{x2} - \mu_{x3})R_{x3}] + W\frac{d_{x1}}{R_{x1}} + F_{fx2} \end{aligned} \tag{36}$$

The hysteretic behavior of the MTFPS isolator in this stage is shown in Fig. 11.

By observing the mobilized force and the displacement at each sliding interface from stage I to stage IV, we can find the regularities and further infer the regular pattern of an MTFPS isolator with several intermediate sliding plates. If the isolation system has N number of sliding interfaces and by assuming the following conditions: (a) $R_{x1} > R_{x2} > R_{x3} > \ldots > R_{xj} > \ldots > R_{xN}$, (b) $\mu_{x1} > \mu_{x2} > \mu_{x3} > \ldots >$

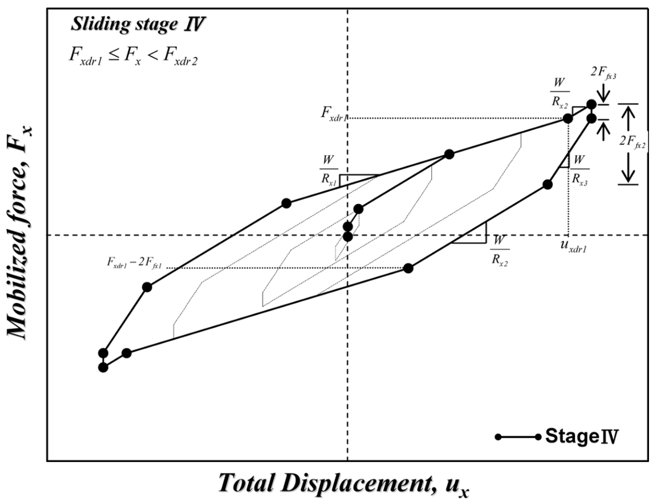

Fig. 11 Force-displacement relationship of the MTFPS isolator during Stage IV

$\mu_{xj} > \ldots > \mu_{xN}$, and (c) $d_{xi} > (\mu_{x(i-1)} - \mu_{xi})R_{xi}$, the following equations can be obtained.

When the sliding motion occurs on the *j*-th sliding interface without contacting the displacement restrainer, the first to the (*j*-1)-th sliding interfaces remain standing still without any movement. The (*j*+1)-th sliding interface to the *N*-th sliding interfaces have already stopped, and the displacement in each sliding interface is expressed as follows

$$\text{When } 1 \le i < j,\; u_{xi} = 0;\text{ and} \tag{38}$$

$$\text{When } j < i \le N,\; u_{xi} = (\mu_{x(i-1)} - \mu_{xi})R_{xi} \tag{39}$$

The mobilized force is given by

$$F_x = \frac{W}{R_{xj}}[u_x - u_{x1} - u_{x2} - \ldots - u_{x(j-1)} - u_{x(j+1)} - \ldots - u_{xN}] + F_{fxj}$$

$$= \frac{W}{R_{xj}}[u_x - (\mu_{xj} - \mu_{x(j+1)})R_{x(j+1)} - (\mu_{x(j+1)} - \mu_{x(j+2)})R_{x(j+2)} - \ldots - (\mu_{x(N-1)} - \mu_{x(N)})R_{xN}] + F_{fxj}$$

$$= \frac{W}{R_{xj}}u_x + \frac{F_{fxj}(R_{xj} - R_{x(j+1)}) + F_{fx(j+1)}(R_{x(j+1)} - R_{x(j+2)}) + \ldots + F_{fxN}R_{xN}}{R_{xj}} \tag{40}$$

When contact is made with the displacement restrainer on the sliding interface *j*–1, the displacement capacities are reached from the first to the (*j*–1)-th sliding interfaces. The sliding motion occurs on the *j*th sliding interface, and the displacement in each sliding interface is expressed as

$$\text{When } 1 \le i < j,\; u_{xi} = d_{xi};\text{ and} \tag{41}$$

$$\text{When } (j+1) \le i \le N,\; u_{xi} = (\mu_{x(i-1)} - \mu_{xi})R_{xi} \tag{42}$$

and the mobilized force can be expressed as follows

$$F_x = \frac{W}{R_{xj}}[u_x - u_{x1} - u_{x2} - \ldots - u_{x(j-1)} - u_{x(j+1)} - \ldots - u_{xN}] + W\left(\frac{d_{x1}}{R_{x1}} + \frac{d_{x2}}{R_{x2}} + \ldots + \frac{d_{x(j-1)}}{R_{x(j-1)}}\right) + F_{fxj}$$

$$= \frac{W}{R_{xj}}[u_x - d_{x1} - d_{x2} - \ldots - d_{x(j-1)} - (\mu_{x(j)} - \mu_{x(j+1)})R_{x(j+1)} - \ldots - (\mu_{x(N-1)} - \mu_{xN})R_N]$$

$$+ W\left(\frac{d_{x1}}{R_{x1}} + \frac{d_{x2}}{R_{x2}} + \ldots + \frac{d_{x(j-1)}}{R_{x(j-1)}}\right) + F_{fxj} \tag{43}$$

Similarly, by following the same procedures as those corresponding to Eqs. (1)-(43) in the *X* direction, mathematical formulations in the *Y* direction can be obtained. This means that by neglecting frictional forces from the walls of the intermediate sliding plates, the proposed MTFPS isolator with numerous intermediate sliding plates will move independently in two orthogonal directions. Accordingly, the natural period and damping effect of the isolator in each direction will change at various stages during earthquakes.

3. Component tests of the MTFPS isolator

The mathematical formulations derived in the previous section are suitable for the cases of an MTFPS isolator with an arbitrary number (N number) of sliding interfaces in each direction, which represent many possible combinations of various features of the sliding interfaces from two directions, including the number of the sliding interfaces, friction coefficients, effective radii, and displacement capacities on the sliding interfaces in each direction. The aim of this section is to examine the mechanical characteristics of the MTFPS isolator by performing the component tests of this device with two sliding interfaces in each direction, which is one of the possibilities of the general formulations presented in the previous section. Fig. 12 shows the exploded view of the MTFPS isolator in the X direction for the component tests, which included two sliding interfaces. Table 1 lists the properties of the MTFPS isolator in the X direction. Fig. 13 shows the picture for the side view of the specimen, and Fig. 14 pictures the overall view of the test set-up for the component tests. Fig. 15 displays the total displacement histories of the isolator in the X direction. The vertical load was 1177.2 kN for the component tests. Fig. 16 gives the displacements of the entire isolator and each sliding interface. Note that while the outer sliding interface was sliding, the inner sliding interface was almost motionless.

In addition, at the moment of contact being made with the displacement restrainer on the outer sliding interface, the intermediate sliding plate bounced back suddenly due to the impact between

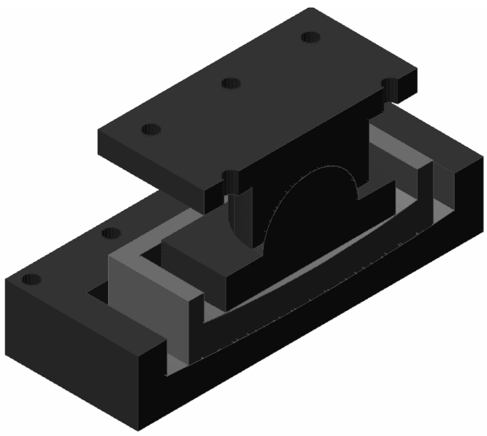

Fig. 12 Exploded view of the MTFPS isolator in the X direction for component tests

Table 1 Properties of the MTFPS isolator for component tests

	X-direction	
Sliding Interface	Outer (1st)	Inner (2nd)
Radius (mm)	3000	1500
Natural Period (sec)	3.475	2.457
Displacement Capacity	40 mm	40 mm
Contact Area (cm^2)	1355.9	441.0
Minimum Friction Coefficient	0.0443	0.03955
Maximum Friction Coefficient	0.1309	0.1157

Fig. 13 Specimen of the MTFPS isolator in the X direction for the component test

Fig. 14 Test set-up for the component test of the MTFPS isolator

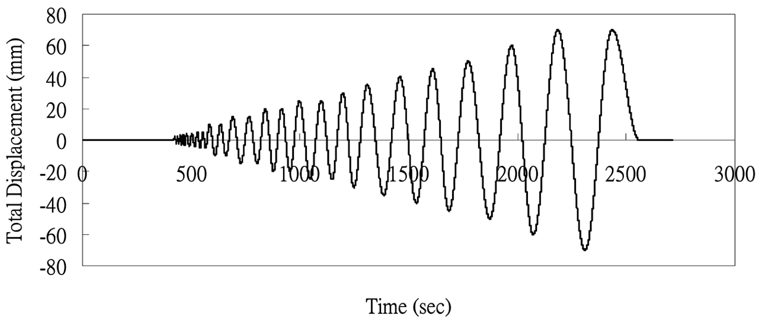

Fig. 15 Displacement histories in the X direction for the component test

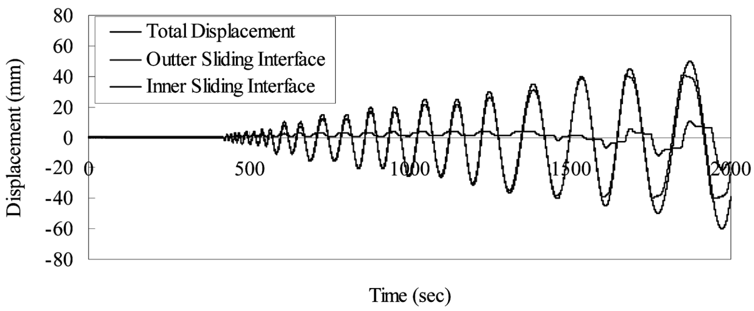

Fig. 16 Displacement histories on each sliding interface

the sliding plate and the restrainer, and the inner sliding interface increased its sliding displacement abruptly to maintain the specified displacement of the entire isolator, yielding larger sliding velocity and friction coefficient on the inner sliding interface. Furthermore, the direction of the frictional force on the outer sliding interface was suddenly changed due to the action of the back bounce. Reasons stated above explained the abrupt change of the horizontal force at the moment of contact

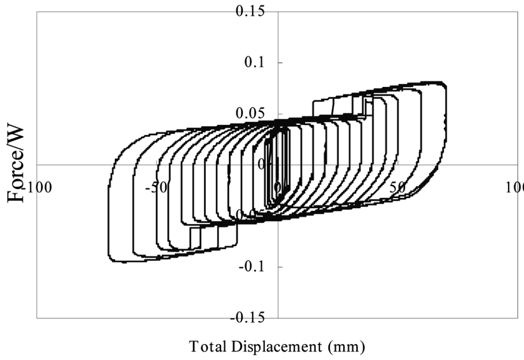

Fig. 17 Hysteresis loop of the MTFPS isolator in the *X* direction

occurrence, as depicted in Fig. 17. Fig. 17 displays the hysteresis loop of the isolator in the *X* direction. The transition of the sliding motions from the inner sliding interface to the outer one was observed during the component tests. During the tests, the isolator started sliding on the inner sliding interface once the horizontal force overcame the frictional force on this interface, which had least friction coefficient. The stiffness was equal to the vertical load divided by the effective radius of the inner sliding interface. The sliding motion was governed by the inner sliding interface after the displacement capacity of the outer sliding interface was reached, and the stiffness was equal to the vertical load divided by the effective radius of the inner sliding interface. These experimental results validate the formulations proposed in the previous section without considering the effect of velocity dependence on sliding coefficients. However, the velocity dependence of friction coefficients on the sliding interfaces was observed in the tests. Therefore, smoother transitions between different stages of sliding motions were observed in the experiments as compared to those obtained from the theoretical formulations derived in the previous section and presented in Figs. 6-11. Experimental observations from the component tests indicate that the velocity dependence on friction coefficients and the impact characteristic between the sliding plate and restrainer at the moment of contact occurrence play important roles on the sliding characteristics of multiple sliding interfaces, and should be taken into account in the mathematical models in the future studies. On the other hand, we may install a buffer such as rubber snubbers or viscoelastic materials between the sliding plates and the displacement restrainers to minimize the impact.

4. Analytical analyses and validation of proposed mathematical model

To investigate the characteristic of the proposed MTFPS isolation system and examine the accuracy of the proposed mathematical model, a MTFPS-isolated system with a rigid mass was tested and simulated while subjected to bidirectional harmonic ground displacements. There were totally four sliding interfaces in the tested MTFPS isolator, two in each direction. The radii of curvature of the first and second sliding interfaces were 3000 and 4473 mm, respectively, for both the *X* and *Y* directions. Fig. 18 shows the time history of the bidirectional ground displacements for the conducted experiment. Figs. 19 and 20 give the calculated friction coefficients on the sliding interfaces in the *X* and *Y* directions, respectively, which are a function of sliding velocities on

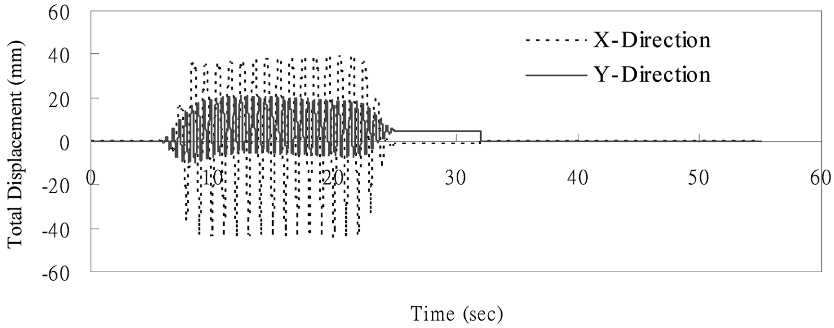

Fig. 18 Ground displacements in X and Y directions

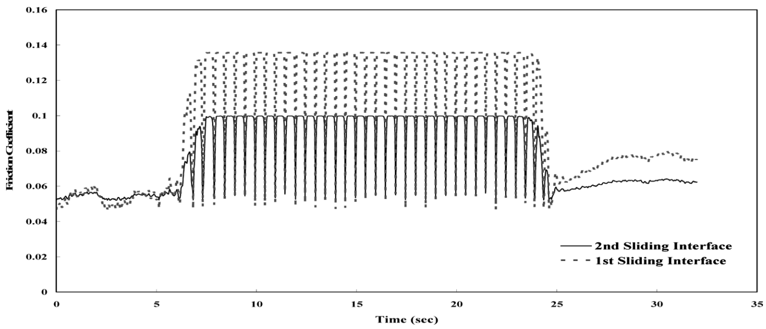

Fig. 19 Time history of friction coefficients on sliding interfaces in X direction while subjected to bidirectional harmonic ground displacements

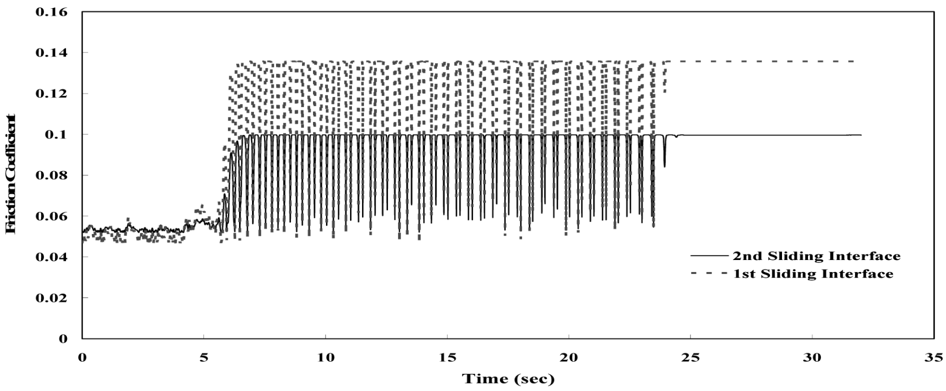

Fig. 20 Time history of friction coefficients on sliding interfaces in Y direction while subjected to bidirectional harmonic ground displacements

sliding interfaces and calculated from measured displacements if the displacement was assumed to be dominated by the individual sliding interface. The sliding velocities were quickly and mostly approached their attenuated values of maximum friction coefficients during the tests (Tsai *et al.* 2005, 2006); therefore, a constant value of the maximum friction coefficient on each sliding interface, which were 0.1357 and 0.09976 for the first and second sliding interfaces, respectively,

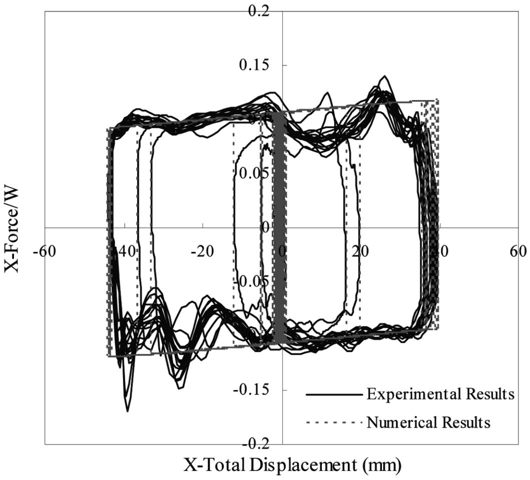

Fig. 21 Comparison of experimental and analytical hysteresis loops in X direction while subjected to bidirectional harmonic ground displacements

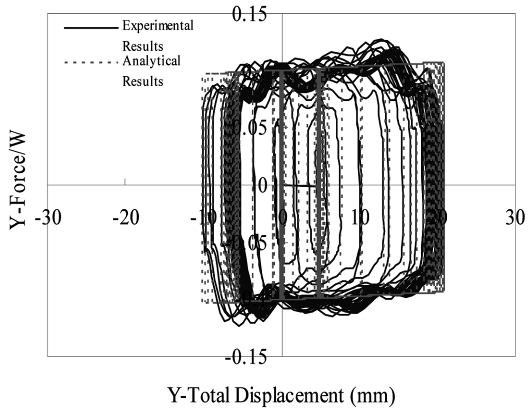

Fig. 22 Comparison of experimental and analytical hysteresis loops in Y direction while subjected to bidirectional harmonic ground displacements

was adopted for the numerical simulations in this study. Figs. 21 and 22 give the comparisons between the analytical and experimental results in the X and Y directions, respectively. As we can see from these two figures, the analytical result is quite consistent with experimental result even a velocity independent friction coefficient on each sliding interface was assumed during numerical calculations. However, no obviously sharp change in stiffness at different stages as we expected in the mathematical modeling was observed during the testing due to the fact of velocity dependent friction coefficients on the sliding interfaces involved in the real tests.

In addition, an analytical comparison has been made between the proposed multiple trench friction pendulum system (MTFPS) and the multiple friction pendulum system (MFPS) with several sliding interfaces invented by Tsai (2002) (Tsai *et al.* 2008, 2010b) and termed the triple friction pendulum bearing by Fenz and Constantinou (2008) if only four sliding interfaces are included in the system. In the given example, a rigid mass system isolated with these two types of isolation devices was subjected to bidirectional harmonic ground accelerations of 0.3 g sin$2\pi t$ in the X direction and 0.3 g sin$2\pi t$ in the Y direction. In the dynamical analyses, the MTFPS and MFPS isolation systems each having eight sliding interfaces (four trench concave surfaces in each direction for the MTFPS and eight spherical concave surfaces for the entire MFPS), four above the articulated slider and another four below the articulated slider, were given as an example for comparisons. Note that material properties for the sliding interfaces above the articulated slider were identical to those for the sliding interfaces below the articulated slider. For sliding interfaces above the articulated slider, the friction coefficients were 0.08, 0.06, 0.04 and 0.02 from the first to fourth sliding interfaces, respectively; the radii of curvature of the first to fourth sliding interfaces were 6.212, 3.976, 2.236 and 0.994 meters, respectively; the displacement capacities on the first to fourth sliding interfaces were 0.2, 0.3, 0.4 and 1.5 meters, respectively. Figs. 23 and 24 show the hysteresis loops of the MTFPS isolator in the X and Y directions, respectively, while Figs. 25 and 26 display the hysteresis loops of the MFPS isolator in the X and Y directions, respectively. If the radii of the trench sliding interfaces

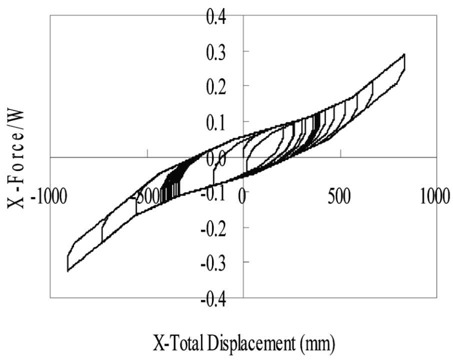

Fig. 23 Hysteresis loop of MTFPS isolator in *X* direction while subjected to bidirectional harmonic ground accelerations

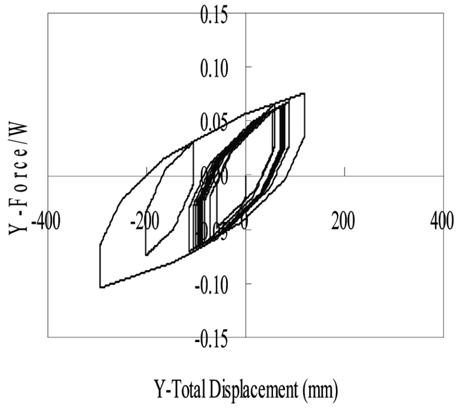

Fig. 24 Hysteresis loop of MTFPS isolator in *Y* direction while subjected to bidirectional harmonic ground accelerations

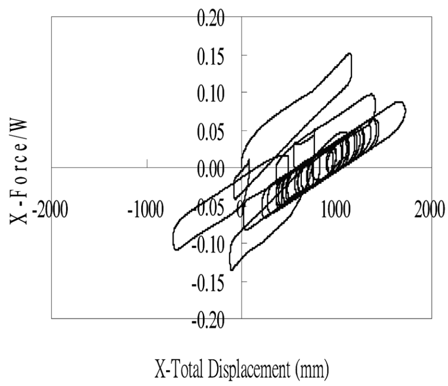

Fig. 25 Hysteresis loop of MFPS isolator in *X* direction while subjected to bidirectional harmonic ground accelerations

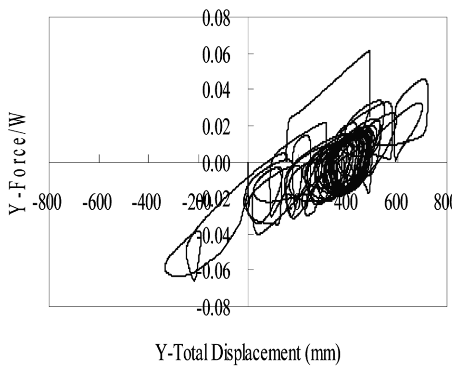

Fig. 26 Hysteresis loop of MFPS isolator in *Y* direction while subjected to bidirectional harmonic ground accelerations

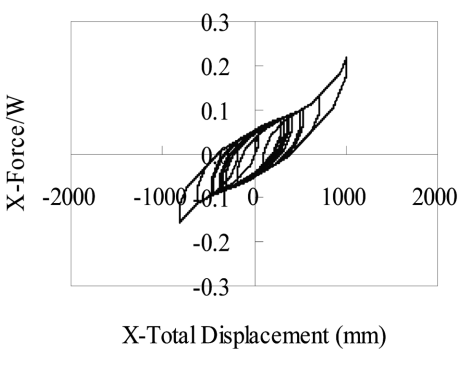

Fig. 27 Hysteresis loop of MTFPS isolator with doubled radii in *X* direction while subjected to bidirectional harmonic ground accelerations

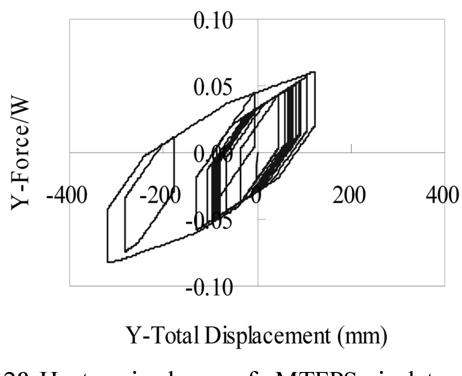

Fig. 28 Hysteresis loop of MTFPS isolator with doubled radii in *Y* direction while subjected to bidirectional harmonic ground accelerations

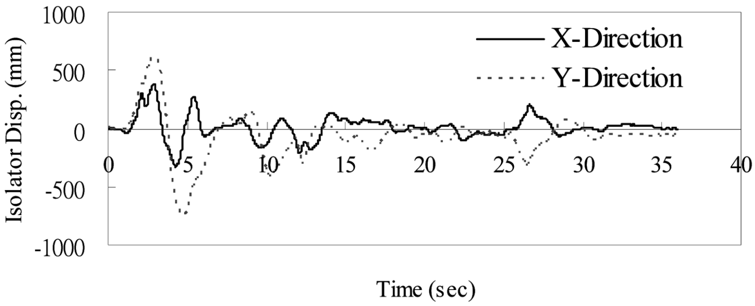

Fig. 29 Time history of MTFPS isolator displacements in X and Y directions while subjected to 1940 El Centro earthquake (X = 1.0 g, Y = 0.6 g in PGA)

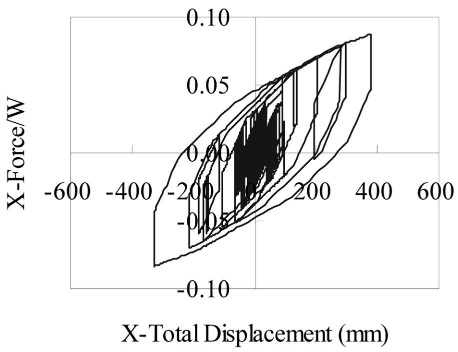

Fig. 30 Hysteresis loop of MTFPS isolator in X direction while subjected to 1940 El Centro earthquake (X = 1.0 g, Y = 0.6 g in PGA)

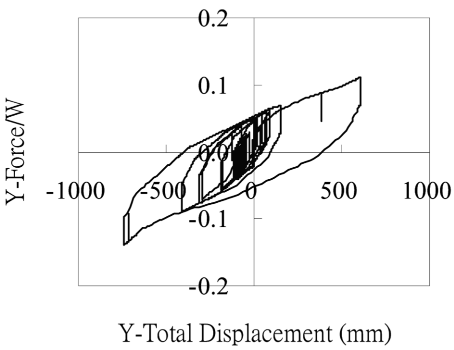

Fig. 31 Hysteresis loop of MTFPS isolator in Y direction while subjected to 1940 El Centro earthquake (X = 1.0 g, Y = 0.6 g in PGA)

in the MTFPS isolator were doubled, similar to the properties of the given MFPS isolator in terms of the isolation period, the hysteresis loops in the X and Y directions of the isolation system are then shown in Figs. 27 and 28, respectively. Comparisons of these figures reveal that the MTFPS isolator possess quite different features from those of the MFPS isolator although the only physical difference between these two isolation systems is the coupling and uncoupling of the sliding motions in two horizontally orthogonal directions on the sliding interfaces. Numerical results from dynamic analyses demonstrate that the MTFPS isolator had greater horizontal force responses with significant reduction in displacement responses while compared to those of the MFPS isolator. Furthermore, Fig. 29 shows the time history of isolator displacements in the X and Y directions, and Figs. 30 and 31 show hysteresis loops in the X and Y directions, respectively, while the MTFPS-isolated system was subjected to a bidirectional El Centro earthquake (1940) with PGAs of 1.0 g and 0.6 g in X and Y directions, respectively.

5. Shaking table tests on a three- story steel structure isolated with MTFPS isolators

In order to examine the efficiency of the proposed isolator on seismic mitigation, a series of shaking table tests on a three-story scaled steel structure isolated with MTFPS were performed in the Department of Civil Engineering, Feng Chia University, Taichung, Taiwan. The sizes of the three-story steel structure were 1.1 m × 1.1 m on the horizontal plane and 2.7 m in height. The cross-section of the column on each floor was H100 × 50 × 5 × 7 mm. In order to simulate inertial forces on each floor, an additional mass of 400 kg was added on each floor. The total mass, including the mass of the structure and added masses, was approximately 2.0 tons, as shown in Fig. 32. In the experiment, selected ground motions including the El Centro (US, 1940), Kobe (Japan, 1995), and Chi-Chi earthquakes (the TCU084 station, Taiwan, 1999) were selected as inputs. The PGAs of the input ground motions varied from 0.2 g to 0.6 g. An MTFPS isolator was installed at the bottom of each column. The MTFPS isolator used in this test had one trench concave surface and one intermediate sliding plate to form two sliding interfaces in each direction. The radii of curvature of the first and second sliding interfaces were 1 m and 0.5 m, respectively. The friction coefficients at low velocities for the first and second sliding interfaces were 0.037 and 0.0356, respectively, and 0.107 and 0.103 at high velocities for the first and second sliding interfaces, respectively. The accelerometers and the displacement transducers (LVDT) were deployed at each floor and the shaking table to measure the structural responses and ground motions.

Figs. 33-35 display comparisons between the roof acceleration responses of the fixed-base and MTFPS-isolated structures under the El Centro, Kobe and Chi-Chi (TCU084 station) earthquakes with 0.6 g in PGA, respectively. From these figures, it can be observed that the MTFPS isolator can significantly reduce structural responses by lengthening the natural period of the entire system and by supplying additional damping under various types of ground motions. The hysteresis loops of the MTFPS isolator under various earthquakes are shown in Figs. 36-38. The enclosed area of the hysteresis loop provides the damping effect to minimize the structural response and the isolator displacement. As explained in Section 3, no obviously sharp change in stiffness at different stages was observed in Figs. 36-38 because the friction coefficients on sliding interfaces were velocity dependent in the shaking table tests, which was not considered in the mathematical modeling in this

Fig. 32 A three story steel structure isolated with four MTFPS isolators

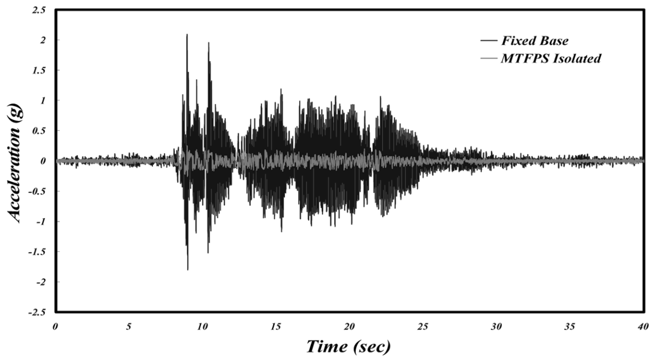

Fig. 33 Comparison of roof acceleration responses of fixed-base and MTFPS-isolated structures under El Centro earthquake with 0.619 g in PGA

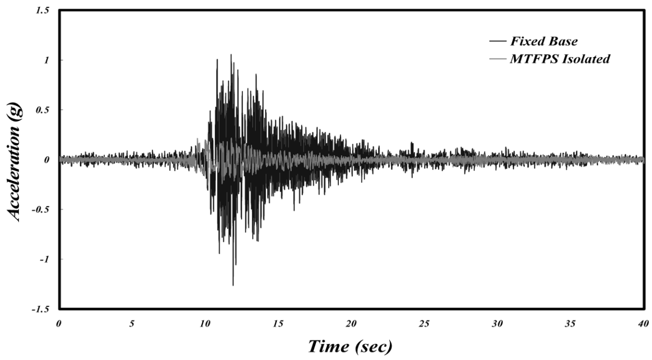

Fig. 34 Comparison of roof acceleration responses of fixed-base and MTFPS-isolated structures under Kobe earthquake with 0.602 g in PGA

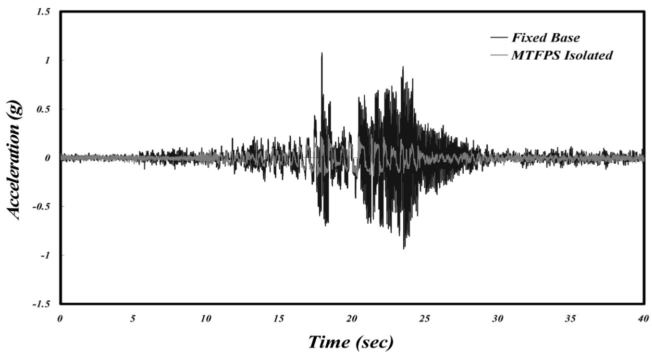

Fig. 35 Comparison of roof acceleration responses of fixed-base and MTFPS-isolated structures under Chi-Chi earthquake with 0.540 g in PGA

study. The test results indicate that the proposed isolator can isolate and absorb earthquake-induced energy. Figs. 39-41 show the displacement time history of the MTFPS isolator when subjected to various earthquakes. It is demonstrated from these figures that negligible residual displacements are observed after earthquakes. Table 2 summarizes the comparisons between the roof acceleration

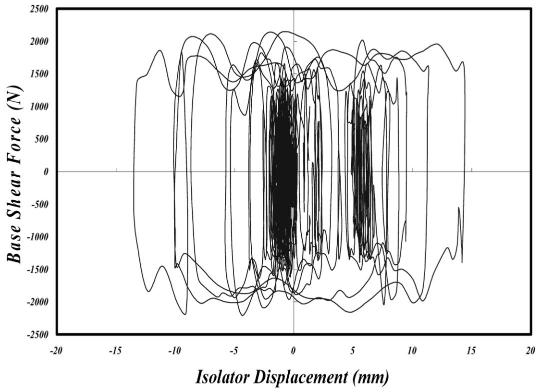

Fig. 36 Hysteresis loops of base isolator under El Centro earthquake with 0.619 g in PGA

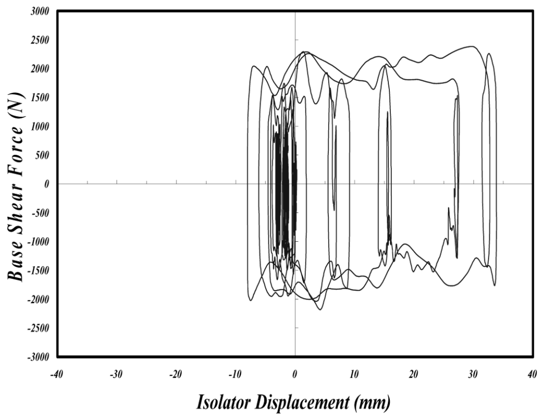

Fig. 37 Hysteresis loops of base isolator under Kobe earthquake with 0.602 g in PGA

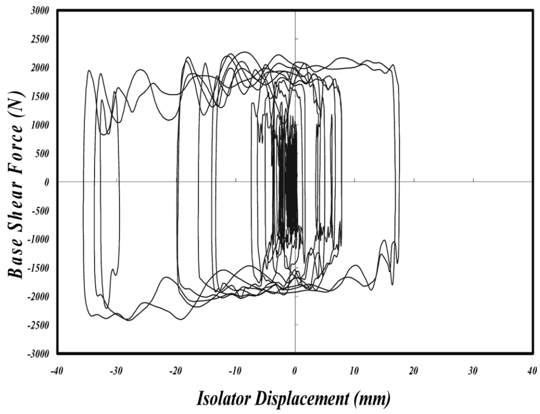

Fig. 38 Hysteresis loops of base isolator under Chi-Chi earthquake with 0.540 g in PGA

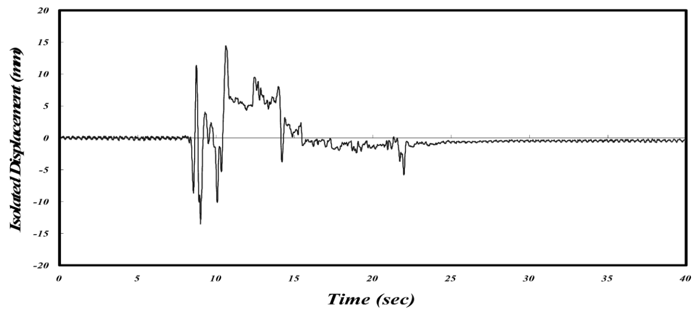

Fig. 39 Time history of isolator displacement under El Centro earthquake with 0.619 g in PGA

responses of the fixed-base and MTFPS-isolated structures. The higher the intensity of the ground motion, the better will be the efficiency of the MTFPS isolator to reduce structural responses. It is also illustrated that the proposed MTFPS isolator is a promising tool for seismic mitigation of structures.

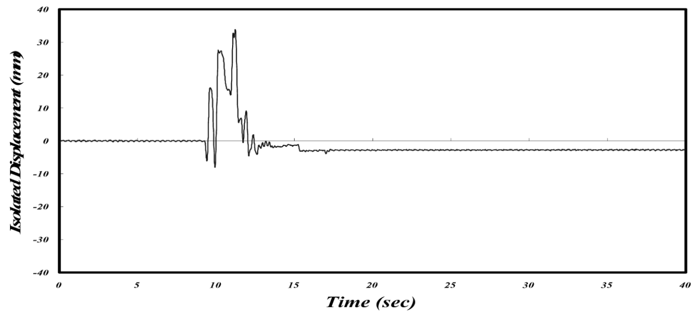

Fig. 40 Time history of isolator displacement under Kobe earthquake with 0.602 g in PGA

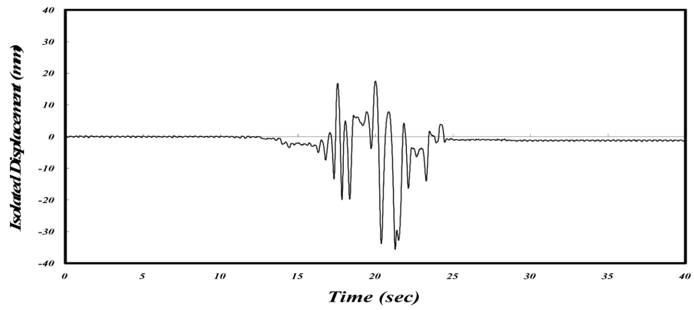

Fig. 41 Time history of isolator displacement under Chi-Chi earthquake with 0.540 g in PGA

Table 2 Comparison of roof acceleration responses of the fixed-base and MTFPS-isolated structures

Earthquakes	PGA (g)	Fixed-Base Structure (g)	MTFPS-Isolated Structure (g)	Response Reduction
El Centro	0.182	0.613	0.168	72.60%
	0.301	1.012	0.232	77.12%
	0.564	1.900	0.236	87.58%
	0.619	2.085	0.285	86.31%
Kobe	0.186	0.391	0.182	53.52%
	0.279	0.585	0.203	65.29%
	0.357	0.749	0.211	71.76%
	0.602	1.264	0.259	79.50%
Chi-Chi (TCU084)	0.196	0.391	0.170	56.67%
	0.338	0.673	0.192	71.53%
	0.399	0.796	0.234	70.55%
	0.540	1.076	0.242	77.49%

6. Conclusions

The characteristics of the proposed multiple trench friction pendulum system with numerous intermediate sliding plates are generally functions of radii and friction coefficients of the trench concave surface and intermediate sliding plates in each direction. The new system provides large flexibility of serving different designing requirements for engineers. The MTFPS isolator moving independently in two orthogonal directions can provide different natural periods, displacement capacities, and damping effects in each direction. The natural period and damping effect of the MTFPS isolator with numerous intermediate sliding plates can change continually during earthquakes. This might avoid the possibility of resonance induced by the ground motions. The shaking table test results demonstrate that the proposed MTFPS isolator can reduce structural responses significantly and that the MTFPS isolator is a promising tool for protection of structures from earthquake damage.

References

Al-Hussaini, T.M., Zayas, V.A. and Constantinou, M.C. (1994), "Seismic isolation of multi-story frame structures using spherical sliding isolation systems", NCEER Technical Report, NCEER-94-0007.

Fenz, D.M. and Constantinou, M.C. (2008), "Spherical sliding isolation bearings with adaptive behavior: Theory", *Earthq. Eng. Struct. D.*, **37**, 168-183.

Jangid, R.S. (2005), "Optimum friction pendulum system for near-fault motions", *Eng. Struct.*, **27**, 349-359.

Kim, Y.S. and Yun, C.B. (2007), "Seismic response characteristics of bridges using double concave friction pendulum bearings with tri-linear behavior", *Eng. Struct.*, **29**, 3082-3093.

Morgan, T.A. and Mahin, S.A. (2008), "The optimization of multi-stage friction pendulum isolators for loss mitigation considering a range of seismic hazard", *Proceeding of the 14th World Conference on Earthquake Engineering*, Beijing, China, October, Paper No. 11-0070.

Mosqueda, G., Whittaker, A.S. and Fenves, G.L. (2004), "Characterization and modeling of friction pendulum bearings subjected to multiple components of excitation", *J. Struct. Eng.-ASCE*, **130**(3), 433-442.

Murnal, P. and Sinha, R. (2002), "Earthquake resistant design of structures using the variable frequency pendulum isolator", *J. Struct. Eng.-ASCE*, **128**(7), 870-880.

Roussis, P.C. and Constantinou, M.C. (2006), "Uplift-restraining friction pendulum seismic isolation system", *Earthq. Eng. Struct. D.*, **35**(5), 577-593.

Tsai, C.S., Chiang, T.C. and Chen, B.J. (2005), "Experimental evaluation of piecewise exact solution for predicting spherical sliding type isolated structures", *Earthq. Eng. Struct. D.*, **34**(9), 1027-1046.

Tsai, C.S., Chen, W.S., Chiang, T.C. and Chen, B.J. (2006), "Component and shaking table tests for full-scale multiple friction pendulum system", *Earthq. Eng. Struct. D.*, **35**(11), 1653-1675.

Tsai, C.S., Lu, P.C., Chen, W.S., Chiang, T.C., Yang, C.T. and Lin, Y.C. (2008), "Finite element formulation and shaking table tests of direction-optimized friction pendulum system", *Eng. Struct.*, **30**, 2321-2329.

Tsai, C.S., Chen, W.S. and Chiang, T.C. (2010a), "Experimental and numerical studies of Trench Friction Pendulum System", *Struct. Eng. Mech.,* **34**(2), 277-280.

Tsai, C.S., Lin, Y.C. and Su, H.C. (2010b), "Characterization and modeling of multiple friction pendulum isolation system with numerous sliding interfaces", *Earthq. Eng. Struct. D.*, **39**, 1463-1491.

Zayas, V.A., Low, S.S. and Mahin, S.A. (1987), "The FPS earthquake resisting system report", EERC Technical Report, UBC/EERC-87/01.

Zayas, V.A., Low, S.S. and Mahin, S.A. (1990), "A Simple pendulum technique for achieving seismic isolation", *Earthq. Spectra*, **6**(2), 317-333.